Practical aspects of applied optimised survey design for Electrical Resistivity Tomography

(Abbreviated title: Applied optimised ERT survey design)

Paul B. Wilkinson[1], Meng Heng Loke[2], Philip I. Meldrum[1], Jonathan E. Chambers[1],

Oliver Kuras[1], David A. Gunn[1], and Richard D. Ogilvy[1]

[1]British Geological Survey, Kingsley Dunham Centre, Keyworth, Nottingham,

NG12 5GG, UK. Email: pbw@bgs.ac.uk

[2]Geotomo Software, 115 Cangkat Minden Jalan 5, Minden Heights, 11700 Gelugor,

Penang, Malaysia.

Abstract

The use of optimised resistivity tomography surveys to acquire field data imposes extra constraints on the design strategy beyond maximising the quality of the resulting tomographic image. In this paper, methods are presented to 1) minimise electrode polarisation effects; 2) make efficient use of parallel measurement channels; and 3) incorporate data noise estimates in the optimisation process. 1) A simulated annealing algorithm is used to rearrange the optimised measurement sequences to minimise polarisation errors. The method is developed using random survey designs, and is demonstrated to be effective for use with single and multi-channel optimised surveys. 2) An optimisation algorithm is developed to design surveys by successive addition of multi-channel groups of measurements rather than individual electrode configurations. The multi-channel surveys are shown to produce results nearly as close to optimal as equivalent single channel surveys, while reducing data collection times by an order of magnitude. 3) Random errors in the data are accounted for by weighting the electrode configurations in the optimisation process according to a simple error model incorporating background and voltage-dependent noise. The use of data weighting produces optimised surveys that are more robust in the presence of noise, while maintaining as much of the image resolution of the noise-free designs as possible. All the new methods described in this paper are demonstrated using both synthetic and real data, the latter having been measured on an active landslide using a permanently installed geoelectrical monitoring system.

Keywords: Inverse theory; Tomography; Numerical approximations and analysis; Electrical properties

1 Introduction

Automatic multi-electrode multi-channel Electrical Resistivity Tomography (ERT) instruments have enabled rapid and flexible collection of data for electrical imaging of the near surface. The availability of such systems has stimulated recent research into optimal survey design algorithms for ERT (see Wilkinson *et al.* 2006a; Coles and Morgan 2009; Maurer *et al.* 2010 for a general overview and specific references). When compared to standard survey designs, such as the dipole-dipole or Wenner-Schlumberger arrays, these algorithms substantially improve the resolution of ERT images while still using the same number of measurements (Stummer *et al.* 2004; Wilkinson *et al.* 2006b; Loke *et al.* 2010a; 2010b). Several different approaches have been proposed to maximise resistivity image resolution including: reconstructing comprehensive data sets from a linearly independent complete subset (Lehmann 1995; Zhe *et al.* 2007; Blome *et al.* 2011); maximising a sum of the Jacobian sensitivity matrix elements (Furman *et al.* 2004; 2007); maximising a sum of the model resolution matrix elements (Stummer *et al.* 2004; Wilkinson *et al.* 2006a; Loke *et al.* 2010a; 2010b); minimising an average measure of the point spread function (Loke *et al.* 2010b); and maximising the determinant of the normal matrix (Coles and Morgan 2009). Of these, the methods based on the model resolution matrix have probably been the focus of the most research effort. But regardless of the optimisation method, generally very little attention has been paid to the additional design constraints that arise when applying optimised surveys in the field. These constraints are: the avoidance of electrode polarisation effects; the efficient use of multiple measurement channels; the presence of noise in the data; and the desirability of making reciprocal measurements to assess noise levels. The notable exception is Blome *et al.* (2011)

who present a practical method for recording a low-noise complete pole-bipole dataset with a multi-channel system

In this paper we address three of these practical restrictions. We present a method to rearrange the order in which the optimised data are measured so that electrode polarisation effects are avoided. We also extend the "Compare *R*" (CR) method of Wilkinson *et al.* (2006a) to make full use of multiple measurement channels, thereby designing near-optimal datasets that can be collected much more quickly than those generated with the existing algorithm. Lastly, we modify the core of the CR algorithm to incorporate error estimates, producing survey designs that are more robust in the presence of random noise. We test the new algorithms using both synthetic data and real measurements made using a permanently installed time-lapse resistivity monitoring system on an active landslide. While this work specifically focuses on adapting the CR method, the approaches that we have used are generic and should be applicable to any of the aforementioned optimal survey design algorithms.

2 The "Compare *R*" method

The optimisation strategy used in this paper makes use of the model resolution matrix **R**, which quantifies the degree to which each model cell in the resistivity image can be resolved by the measured data. For the linearised least-squares inversion method, the relationship between the measured data and the model cell resistivities is given by

$$(\mathbf{G}^{\mathrm{T}}\mathbf{G} + \mathbf{C})\Delta\mathbf{r}_i = \mathbf{G}^{\mathrm{T}}\mathbf{d} - \mathbf{C}\mathbf{r}_{i-1}, \tag{1}$$

where the Jacobian matrix **G** comprises the logarithmic sensitivities of the measurements to changes in the model cell resistivities, the constraint matrix **C** contains the damping factors and roughness filters, **d** is the data discrepancy vector,

$\mathbf{r}_{i-1}$ is the vector of logarithms of the model resistivities from the previous iteration, and $\Delta\mathbf{r}_i$ is the change in model parameters for this iteration. The model resolution matrix (Menke 1989) for this formulation is given by

$$\mathbf{R} = (\mathbf{G}^{\mathrm{T}}\mathbf{G} + \mathbf{C})^{-1}\mathbf{G}^{\mathrm{T}}\mathbf{G}. \qquad (2)$$

The leading diagonal elements of $\mathbf{R}$ give an estimate of the resolution of the individual model cells, which we call the "model resolution" and denote R. The model resolution takes values $0 \le R \le 1$ (Wilkinson *et al.* 2006a), where 0 is unresolved and 1 is perfectly resolved. The model resolution is maximal throughout the image space for the comprehensive measurement set, which comprises all possible unique four-electrode measurements. To improve the stability of the inversion in the presence of noise, the comprehensive set is reduced by removing the Wenner-γ type measurements and all others with geometric factors greater than a prescribed limit (Wilkinson *et al.* 2006a).

The CR method attempts to find a survey design that maximises the average model resolution for a given number of measurements much smaller than the size of the comprehensive set. For practicality, it uses a locally-optimal successive design algorithm rather than a global optimisation method. In this approach, introduced by Stummer *et al.* (2004) and improved by Wilkinson *et al.* (2006a), all possible measurements are ranked in order of the estimated improvement which they would make to the model resolution of a baseline measurement set. Several highly ranked measurements are then included in the set, the model resolution is recalculated, and the process is iterated until the survey contains the desired number of measurements. The estimates of the model resolution changes depend on scaled sums of sensitivities, which can be calculated efficiently since their computational cost scales linearly with the number of model cells. Wilkinson *et al.* (2006a) demonstrated that significantly

greater model resolutions could be achieved by calculating the change in the model resolution, ΔR, exactly. While calculating R scales with the cube of the number of cells, calculating ΔR scales as its square if the Sherman-Morrison Rank-1 update is used. This approach is therefore still practical to use for optimal survey design in 2.5D. By reimplementing the original CR algorithm to take advantage of modern cache architecture and parallel processing capabilities, Loke *et al.* (2010a; 2010b) demonstrated that using this method was feasible for up to 60 electrodes. We have since found that, on a 64-bit platform with sufficient memory, optimisation of any realistic (i.e. up to a few hundred electrodes) 2.5D survey should be possible. A version of the parallelised CR algorithm is used throughout this paper, and was implemented using the GotoBLAS2 accelerated Basic Linear Algebra Subroutines libraries (Goto & van de Geijn 2008).

In the original formulation of the CR method, the configurations are ranked in terms of $\sum_{j=1}^{m} \frac{\Delta R_b(j)}{R_b(j)}$, where R_b is the resolution of the base set and m is the number of model cells. The highest ranking configuration (with sensitivity vector $\mathbf{g}_1$) is added to the base set at each iteration. The next highest ranked configuration, $\mathbf{g}_2$, is only added if it has a suitable degree of orthogonality to the first, which is assessed by checking that $|\mathbf{g}_1 \cdot \mathbf{g}_2| / (|\mathbf{g}_1| |\mathbf{g}_2|)$ is less than a given linear dependence limit (*lim*). In the original CR method, the best model resolution was found to be given by $lim = 0.97$. This process is repeated until a certain number of configurations have been added (here we used 9% of the size of measurement set at the start of the iteration), after which R is recalculated and the next iteration is begun. The optimisation performance of this method is shown in Figure 1 for a linear array of 32 electrodes, with a base set comprising 159 configurations (dipole-dipole with a = unit electrode spacing and $n = 1a \rightarrow 6a$) and the final set containing 575 configurations. The plots show the average

relative model resolution $S = \frac{1}{m} \sum_{j=1}^{m} \frac{R(j)}{R_c(j)}$, where R is the resolution of the optimised

set and R_c is the resolution of the comprehensive set. The blue curve shows the

performance of the original CR method, and the dashed black curve shows the

resolution achieved by the brute force approach of adding only a single configuration

at each step, which gives the best possible performance for this type of local

optimisation procedure. Since we published the original CR method, we have found

that a slightly modified ranking function $\sum_{j=1}^{m} \frac{\Delta R_b(j)}{R_c(j)}$ produces better results, as shown

by the red curve in Figure 1. We have also found that using a variable linear

dependence limit improves the optimisation performance further. The green curve

shows the results obtained by setting $lim = S$ at the start of each iteration. This

imposes a stricter limit when the size of the array is small causing more advantageous

configurations to be selected, but as the array grows, and the best configurations have

already been added, the limit is relaxed. The combination of these two improvements

brings the performance of the CR method very close to the single-step results, while

maintaining its speed advantage (the single step results took 14 minutes to calculate

on an eight-core Intel Xeon X7560 processor, while the three CR methods each took

32 seconds).

Figure 2 compares the results produced by the new CR method against a

standard dipole-dipole survey configuration. Both consist of 575 measurements, for

the dipole-dipole survey the dipole length was $a = 1 \rightarrow 4$ electrode spacings and the

dipole spacing was $n = 1a \rightarrow 10a$, while the optimised survey was as described above

for Figure 1. The electrode spacing was 4.75 m and in both cases the maximum

permitted geometric factor was $K_{max} = 39\,396$ m (equivalent to $a = 9.5$ m, $n = 10a$).

For simplicity, the constraint matrix was chosen to represent a simple damped

(Levenberg-Marquardt) least-squares problem, $\mathbf{C} = \lambda \mathbf{I}$ (Loke *et al.* 2010b found no

8

significant differences between using damping or smoothness constraints). The damping factor $\lambda = 0.001$ was chosen so that the model resolution was small ($R \approx 0.05$) at the base of the image (in general higher damping factors reduce the model resolution; see Loke *et al.* 2010a for a detailed discussion). The model resolution distribution across the imaging region for the comprehensive set is shown in Figure 2a. The distribution of the relative model resolution R_r (the model resolution normalised by the comprehensive set model resolution) is shown for the dipole-dipole survey (Figure 2c) and the optimised survey (Figure 2e). The dipole-dipole average model resolution is $S = 0.629$, but the optimised model resolution is significantly greater at $S = 0.717$ for the same number of measurements. Comparing Figure 2e and c shows that the optimised survey produces high relative resolution values throughout the model space, compared to the dipole-dipole survey where the model resolution decreases rapidly towards the sides, corners and base of the image.

We tested the dipole-dipole and optimised surveys against a synthetic model comprising four resistive prisms of $\rho = 100 \, \Omega$m buried at different depths in a background of $\rho = 10 \, \Omega$m (Figure 2b). The data were calculated using the Res2DMod program with a finite-difference forward modelling algorithm. They were inverted with the associated Res2DInv software using the same model cell discretisation and an L_1-norm (blocky) model constraint (Loke *et al.* 2003). Res2DInv used a finite-element method to avoid having the same combination of discretisation and modelling algorithm in the forward and inversion processes. Qualitatively, the optimised inverted image resembles the forward model more closely than the dipole-dipole image. The shapes of the prisms are more accurately recovered (especially that of the deepest prism), and their resistivity contrasts are also closer to the forward model (especially for the right-hand prism). For a more quantitative comparison, we

calculated the Pearson correlation coefficient P and the structural similarity coefficient Σ (Wang & Sheikh 2004) between the forward and inverted models. The Pearson coefficient gives a simple measure of image correlation, whereas the structural similarity coefficient emphasises similarity in structure and contrast. They both give more reliable measures of image similarity than the root-mean-squared difference metric (for details see Wang & Sheikh 2004). Both give the value 0 when comparing the target image to a random image with the same mean and variance, and 1 if the comparison image is identical to the target. For the dipole-dipole image, P = 0.825 and Σ = 0.785, but both coefficients are greater for the optimised image which gives P = 0.837 and Σ = 0.794.

3 Application to field data

When inverting a comprehensive measurement set, there can be significant sensitivity to resistivity variations beyond the ends of the line of electrodes (Maurer and Friedel 2006). Therefore an inversion of a comprehensive set must incorporate these "outer-space" regions in the model. Since the optimised sets are designed to approach the sensitivity of the comprehensive set, their inversions must also account for variations in the resistivity in the outer-space regions. For the synthetic data tests shown in Figure 2 the outer-space was homogeneous, but this will not generally be the case for field data. The extents of the outer-space regions with significant model resolution are shown in Figure 3 for the dipole-dipole and comprehensive sets considered above. The dipole-dipole survey has negligible model resolution in the outer-space (Figure 3a), but Figure 3b shows that significant model resolution values occur up to four electrode spacings (19 m) beyond each end of the line for the

optimised survey. Therefore for testing with field data this region is incorporated into the inversion models.

The field data sets used in this paper were acquired from an active landslide site near Malton, North Yorkshire, UK (Chambers *et al.* 2011). The site is being monitored using an automated time-lapse electrical resistivity tomography (ALERT) system (Wilkinson *et al.* 2010) to study the hydraulics of landslide processes. The ALERT instrument uses wireless telemetry to communicate with an office based PC that runs control software and a database management system. The control software is used to schedule data acquisition, while the database management system stores, processes and inverts the remotely streamed ERT data. The capability that this provides for flexible and remotely configurable data acquisition is ideal for testing optimised survey designs without needing to manually revisit the site.

The research site is located on a south facing valley side with a slope of approximately 14°. The bedrock geology, from the base to the top of the slope, comprises the Lias Group Redcar Mudstone Formation (RMF), Staithes Sandstone and Cleveland Ironstone Formation (SSF), and Whitby Mudstone Formation (WMF), which are overlain at the top of the hill by the Dogger Sandstone Formation. The bedrock is relatively flat lying with a gentle dip of a few degrees to the north, and the strata are broadly conformable (British Geological Survey 1983). Slope failure at the site is occurring in the weathered WMF, which is highly prone to landsliding. The landslide is characterized by shallow rotational failures at the top of the slope that feed into larger-scale slowly moving lobes of slumped material, which extend approximately 150 m down the slope. The data were collected from one of five permanently installed parallel linear electrode arrays running approximately south to north from the base to the top of the hill, each comprising 32 electrodes with along-

line spacings of 4.75 m and inter-line spacings of 9.5 m. The objective of the installation is to visualise and monitor resistivity changes associated with hydraulic precursors to slope failure using time-lapse 3D ERT. The 3D data comprise along-line configurations as well transverse and diagonal cross-line measurements (it is worth noting that there is no evidence of significant anisotropy in the 3D data). However, the structure of the subsurface is such that it is valid to invert the along-line data from individual arrays in 2.5D (Wilkinson *et al.*, 2010) and hence the site is suitable for testing optimised 2.5D survey designs. The selected linear array was chosen to intersect the edge of an active lobe, although it should be noted that the landslide did not move during the acquisition of the data presented in this paper.

The data sets were measured in normal and reciprocal arrangements (Parasnis 1988) for both the dipole-dipole and optimised surveys. For each configuration, the apparent resistivity value was taken to be the mean of the normal and reciprocal measurements. The difference between the measurements was used to calculate the standard error in the mean for each configuration, which we refer to as the reciprocal error. Figure 4 shows the distributions of reciprocal errors and inverted images for the dipole-dipole and optimised surveys. All data were inverted using a model that incorporated an extra 19 m outer-space region at each end, although only the region of the model between the end electrodes is shown. The reciprocal error distribution for the dipole-dipole set is shown in Figure 4a. It peaks at just below 0.1%, and the maximum error is <3%. The inversion used an L_2-norm (smoothness) model constraint and converged after four iterations to an RMS misfit of 1.1%. The inverted image is shown in Figure 4c, and its resistivity structure and variations are consistent with the expected stratigraphic sequence (this is discussed in detail at the end of the section 4).

By contrast, the data for the optimised set exhibited some very large reciprocal errors (in certain cases over 100%, see Figure 4b). These caused the model to converge to a very high RMS misfit of 39.4%; the resulting image is shown in Figure 4d. The cause of the significantly larger data errors in the optimised survey was found to be electrode polarisation, caused by the use of electrodes to measure potential that had previously been used to pass current (Dahlin 2000; Merriam 2005).

4   Minimising polarisation effects

If standard metallic electrodes are used to inject the current for a resistivity measurement, then charges will build up at the metal/earth interfaces. Any potential differences subsequently measured using either or both of these electrodes will be affected by this polarisation as it decays. While non-polarising electrodes can be used to avoid these effects, they are more expensive and difficult to emplace than metal stake electrodes. To permit the use of metallic electrodes, resistivity meters use alternating positive-negative pulse sequences to minimise polarisation errors. This is generally very effective when the decay of the polarisation is approximately linear (Dahlin 2000). But errors will still occur if the duration of the measurement window is similar to the characteristic time-scale of the decay, typically between a few seconds and tens of seconds (Dahlin 2000; Merriam 2005).

Ideally the measurements should be arranged so that during the collection of the data set no electrode is used to measure potential after previously transmitting current. This is easily achieved for a dipole-dipole survey, but for a general survey it is likely that no such arrangement will exist. In that case, it is sufficient to arrange the measurements such that enough time will elapse after a given electrode has transmitted current to let any strongly non-linear polarisation decay occur before the

same electrode is used to measure potential. Dahlin (2000) showed how this can be achieved for a regular structured measurement sequence like a Wenner-based survey. But for a general survey comprising a mixture of the fundamental four-electrode configuration types there will probably be no such natural ordering to exploit.

Despite the ongoing research effort into experimental design for ERT, very little attention has been paid to electrode polarisation. Although Stummer *et al.* (2002) noted that optimised measurement sequences should be designed to avoid polarisation effects, to our knowledge this was not actually implemented in their design algorithms or in any other subsequent work on the subject. The problem was noted again by Loke *et al.* (2010a), who tackled the problem by sorting the four-electrode configurations, which have the form C_1, C_2, P_1, P_2, into ascending electrode order, with P_1 varying most rapidly, then P_2, then C_1, then C_2. After sorting, sections of the configuration list with common C_1 and C_2 electrodes were reversed if any electrode used to measure potentials in that section had been used to pass current within the previous 1, 2 or 3 configurations. While this tended to work well, it is nevertheless easy to envisage cases where it would fail. Also it was designed for single-channel operation and although conceptually easy to extend to multi-channel, the likelihood of multi-channel measurement sets causing it to fail would be much greater.

Here we describe the use of a global minimisation method to rearrange measurement configurations to reduce electrode polarisation effects. The reordering algorithm is generic, suitable for single or multi-channel data collection, and should be applicable to resistivity measurement surveys designed by any algorithm. We assume that a measurement "command" with M channels will involve two electrodes transmitting current and $M + 1$ electrodes measuring M potential differences, which is the method of multi-channel acquisition implemented by the ALERT instrument. The

ith such command will be denoted C_{i1}, C_{i2}, P_{i1}, P_{i2}, …, $P_{i(M+1)}$. To reorder the command sequence we calculate a cost function for its arrangement $c = \Sigma_i(1/d_i)$, where $d_i = j\text{-}i$ and the jth command is the first subsequent command containing a potential electrode that was used as a current electrode in the ith command (i.e. d_i is the smallest positive integer for which $\{P_{j1}, P_{j2}, …, P_{j(M+1)}\} \cap \{C_{i1}, C_{i2}\} \neq \emptyset$). For example, if electrodes 4 and 6 are used to transmit current in command i, and subsequently electrode 4 is used as a potential electrode in command $(i+3)$, then $d_i = 3$. In the case that both current electrodes in command i are not subsequently used to measure potential, we set $1/d_i = 0$. By reordering the commands to minimise c, we aim to maximise the time between any electrode passing current and then subsequently being used to measure potential.

We used a sequence of $n = 64$ randomly generated 10-channel commands to test the reordering algorithms. The cost of this original command sequence was 48.92, and the distribution of C-P separations d is shown by the grey histogram in Figure 5b. To illustrate the challenges of minimising the cost function, we initially generated 64 000 random rearrangements of the commands (10 000 iterations, and 64 rearrangements per iteration). The blue curve in Figure 5a shows the minimum cost found by random reordering as a function of the iteration number. After 10 000 iterations, the minimum cost achieved was 35.32, and the distribution of d was as shown by the blue histogram in Figure 5b. For comparison, the Loke *et al.* (2010a) method produced a cost of 39.23, confirming that it is not well suited to rearranging general multi-channel command sequences.

The optimal reordering of the measurement commands is a combinatorial minimisation problem similar to the well-known "Travelling Salesman" problem. An efficient reordering method in this case is to either move or reverse a randomly

15

selected portion of the sequence (Press *et al.* 1992). Using these more efficient permutations in place of randomly rearranging the entire sequence produced a much reduced minimum cost of 12.19, illustrated by the red curve in Figure 5a and red histogram in Figure 5b. To generate new test sequences, we always permuted the sequence with the minimum cost encountered so far. This gave a rapid improvement in the cost function at the expense of finding a local minimum, which is analogous to rapidly cooling, or quenching, a molten metal. Better results are possible using "simulated annealing", which is a global minimisation method more analogous to slow cooling, which leads to a lower energy state.

To use the simulated annealing method we employed the same combination of reversals and moves, but assigned a "temperature" T to the system that was slowly reduced at each iteration. The initial temperature T_0 was taken to be the standard deviation of the costs of n randomly rearranged sequences. Each new test sequence (of cost c_t) then replaced the currently held sequence (of cost c_0) with probability $p = \exp(-(c_t-c_0)/T)$. Doing so always accepts permutations with lower costs, but will also sometimes accept those that produce higher costs. This allows the algorithm to escape from local minima, but with progressively lower probability as the temperature is reduced. We found that $T = T_0(1-q/Q)^5$ produced reliable results, where q is the iteration number and Q is the total number of iterations. The minimum cost found by this method for the random 64 command sequence was 9.36, shown by the green curve and histogram (Figure 5a and b respectively), and took 3.8 seconds for 10 000 iterations. Note that since the algorithm performs n sequence permutations per iteration, and the time taken to calculate the cost function scales linearly with n, the overall time taken for a sequence with n commands scales as n^2.

To find the best combination of reversals and moves, we conducted 10 trials using only reversals for 14 different maximum permutation lengths (shown as blue squares in Figure 6). We also did the same using only moves (shown as red circles). The results showed that moving a section of the command sequence to a new location in the list was more efficient than reversing a section of the sequence. We then tested a combination of moves and reversals, with a given probability of reversing a section (black crosses in Figure 6). Within error, this produced equally low costs for $0 \leq p_{rev} \lessapprox 0.4$. We arbitrarily chose $p_{rev} = 0.1$ for the results shown in this paper, in combination with a maximum permutation length of 7 for reversals and 1 for moves (N.B. the stated length of a reversed/moved section excludes/includes the first command respectively).

The optimised survey with 575 single channel commands discussed in section 3 had an initial cost of 86.39 and a d value distribution shown by the grey histogram in Figure 7. We found that $Q = 500$ iterations of the simulated annealing procedure were sufficient to reduce the cost to 0.62 with d values shown by the black histogram in a time of 8.5 seconds. For comparison, the Loke *et al.* (2010a) reordering method, which works well for single channel survey designs, produced a cost of 2.94. In the reordered survey, there was a minimum of 82 commands before any current electrode was subsequently used to measure potential, a separation in time equivalent to approximately 11 minutes. The beneficial effects of reordering the survey are shown in Figure 8a, which compares the distributions of reciprocal errors for the original and reordered optimised surveys. After reordering, the distribution peaks at just above 0.1%, and the maximum error is <3%, compared to over 100% in the errors from the original sequence data. While the optimised survey data still has slightly larger reciprocal errors than the dipole-dipole survey (Figure 4a), these are due to the

optimisation procedure tending to select configurations with higher average geometric factors (Loke *et al.* 2010a) rather than being caused by any residual polarisation. The inversion of the data from the reordered optimised survey converged after four iterations to an RMS misfit of 1.2%. The inverted image is shown in Figure 8b and it compares much more closely to the dipole-dipole image (Figure 8c) than the original optimised image does (Figure 4d), both in terms of resistivity structure and RMS misfit.

Both the optimised and dipole–dipole images exhibit resistivity variations consistent with the expected stratigraphic sequence (Figure 8b and c respectively). The boundary between the Whitby and the Staithes formations (WMF and SSF) has been inferred from the resistivity images and is clearly defined in each case. There is also a clear indication in both resistivity images of slipped WMF material overriding the more competent SSF. The lower boundary between the SSF and the Redcar formation (RMF) has been positioned to be consistent with an auger hole log on an adjacent electrode line (Loke *et al.* 2010a). It is clear from Figure 8c that the dipole-dipole image has not captured the SSF/RMF boundary very accurately, whereas it is much more clearly resolved in the optimised survey image (Figure 8b). Within the WMF there are higher surface resistivities in the vicinity of the main scarp that are most likely due to increased localised fracturing. These features also seem more clearly defined in the optimised image. These findings are consistent with the distributions of R_r (Figure 2c and e), which suggest that the optimised survey should produce better resolution than the dipole-dipole survey at depth and towards the edges of the images. In general, careful examination of Figure 8 reveals that the contrast of equivalent features is slightly greater throughout the model space in the optimised

image than in the dipole-dipole image, supporting the findings of section 3 for the synthetic models.

5 Multi-channel optimal survey design

So far the optimisation strategy we have studied has produced output suitable for single channel (SC) measurements. Modern resistivity instruments tend to have multi-channel (MC) capability where several potential differences can be measured for each current dipole. The benefits of MC operation are clear, with M channels data acquisition can be accelerated by a factor of up to M with suitably designed surveys. While some standard electrode configurations (e.g. dipole-dipole) are naturally well-suited to MC operation, optimal survey algorithms must explicitly account for the MC capability of the instrument. Here we present a simple modification of the CR algorithm which should also be applicable to other optimisation methods.

We considered the type of multi-channel operation employed by the ALERT instrument and others (e.g. the AGI SuperSting), although the method would be easy to adapt to other multi-channel implementations. A given multi-channel command has the form $C_1, C_2, P_1, P_2, \ldots, P_{M+1}$, which denotes simultaneous measurement of C_1, C_2, P_1, P_2; C_1, C_2, P_2, P_3; $\ldots$; C_1, C_2, P_M, P_{M+1}. The multi-channel CR (MCCR) optimisation method has the same basis as the original single channel CR algorithm: configurations are ranked by $\sum_{j=1}^{m} \frac{\Delta R_b(j)}{R_c(j)}$ and are tested for linear dependence. But in addition, a set number of MC commands are filled with measurement configurations according to the following procedure:

1. Recalculate ΔR for all unused configurations and sort them in order of descending rank, as for the SC method.

2. Find the next incomplete or empty MC command.

3. If the command is incomplete rather than empty proceed to step 4, otherwise begin the command with the highest-ranked configuration.

4. Find the highest ranked unused configuration that simultaneously: a) satisfies the linear dependence criterion; b) uses the same pair of current electrodes as used in the command; c) has one potential electrode in common with either the first or last potential electrode of the command; d) has its other potential electrode not already in use in the command.

5. Add this configuration to the command and repeat step 4 until either the command is fully populated or the end of the ranked list is reached.

6. Repeat the procedure from step 1 until all commands are fully populated.

In the single channel CR algorithm, the only criterion on subsequently selected commands is the linear dependence test. But in the MCCR algorithm, three additional requirements (4b-d) must also be satisfied. In practice we found that combining these requirements with a variable linear dependence limit (equal to S) caused the optimisation performance to decrease significantly in comparison with the single channel results. The strict initial limit on linear dependence coupled with the additional requirements was causing the algorithm to select configurations that did not contribute greatly to increasing the average model resolution. Therefore in the MCCR algorithm we have reverted to the best performing fixed linear dependence limit $lim = 0.97$, which initially allows the algorithm more freedom to choose from configurations that fit into the commands.

Typically the number of iterations required by MCCR is equal to or slightly greater than the number of commands. This makes the algorithm slower than the single channel CR algorithm (e.g. in the previous SC example 15 iterations of the CR algorithm were used, whereas 50-100 MCCR iterations might be typical for a 32-

electrode array). However, the MCCR method produces survey designs that are nearly as close to optimal as the CR algorithm, with the benefit of exhibiting an order-of-magnitude more rapid data acquisition in the field.

The performance of the MCCR algorithm is demonstrated in Figure 9. We compared the original CR results (Figure 2e and f) with MCCR for two situations, one with the minimum number of commands (58) to accommodate the same number of configurations as the dipole-dipole survey, and one with the same number of commands (98) as the dipole-dipole survey. The first case took 132 s to produce the 58-command survey with 580 configurations. This yielded an average resolution of $S = 0.699$ (Figure 9a) and an inverted image which is qualitatively and quantitatively very similar to that produced by the single-channel survey, having $P = 0.836$ and $\Sigma = 0.794$ (Figure 9b). This survey design contains approximately the same number of measurements as the dipole-dipole survey, but it can be collected in 60% of the time while producing a superior image (with $S = 0.629$, $P = 0.825$, $\Sigma = 0.785$; c.f. Figure 2c and d). In the second case, the MCCR algorithm took 251 s to produce the 98-command survey. This gave $S = 0.751$ (Figure 9c), and an inverted image with $P = 0.845$ and $\Sigma = 0.809$ (Figure 9d). This survey contains 980 measurements, but it can be collected in the same time as the dipole-dipole survey and produces a superior image than either the dipole-dipole or the 58-command survey. The actual times taken to measure the data with the various arrays were: 13 minutes for the dipole-dipole survey; 78 minutes for the SC survey; 8 minutes for the 58-command MCCR survey; and 13 minutes for the 98-command MCCR survey.

To use the MCCR surveys in the field, we rearranged the order of the commands using the simulated annealing approach described in section 4. The distribution of C-P separations before and after reordering are shown in Figure 10a

and b for the 58-command and 98-command surveys respectively. In each case $Q = 500$ iterations were used as with the single channel survey. This took 0.16 s for the 58-command survey, reducing the cost function from 24.08 to 3.13 and increasing the minimum C-P separation from 1 command to 6 commands (Figure 10a). For the 98-command survey reordering took 0.42 s, reducing the cost function from 49.51 to 6.40 and increasing the minimum C-P separation from 1 command to 5 commands (Figure 10b). For comparison, the sorting and reversal method of Loke *et al.* (2010a) produced cost function values of 8.81 for the 58-command survey and 23.88 for the 98-command survey, and in both cases several C-P separations of 1 command remained after reordering.

The effects of rearranging the commands to avoid polarisation effects are demonstrated in Figure 11. The data were collected for both surveys in their original orderings and their rearranged orderings. In addition, reciprocal data were collected for each survey in single channel mode (note that these single channel reciprocal surveys were arranged to avoid polarisation effects in the same manner as described in section 4; the issue of producing multi-channel reciprocal surveys will be discussed in the conclusion). The results of the 58-command survey in its original ordering are shown in Figure 11a and c (reciprocal error distribution and inverted image respectively). As with the original single channel survey the data are strongly affected by electrode polarisation, leading to many large reciprocal errors and poor convergence of the inverted data (RMS misfit = 26.2%). By contrast the reordered 58-command survey has a reciprocal error distribution (Figure 11b) very similar to that of the reordered single channel survey (Figure 8a), and also produces a similar inverted image (Figure 11d) with the same RMS misfit = 1.2%. A detailed comparison of this image with the reordered single channel image (Figure 8b) reveals

that the contrast of the features in the multi-channel case is very slightly lower than in the single channel case, as would be expected since the average model resolution is lower for the 58-command survey than for the single channel survey. However, the improvements over the dipole-dipole image are very similar (see discussion of Figure 8).

The results for the 98-command survey are very similar; before reordering many of the reciprocal errors are high (Figure 11e) and the inverted image is poor (Figure 11g) with a large RMS misfit = 24.2%. After reordering, the reciprocal errors (Figure 11f), inverted image (Figure 11h) and RMS misfit (1.3%) are similar to the reordered single channel data. In this case comparison with the single channel image suggests that the feature contrasts are marginally higher, which is consistent with the higher average model resolution. Again all the previously observed improvements over the dipole-dipole image are present.

6 Incorporating data noise estimates

Once the errors caused by electrode polarisation had been minimised, the remaining levels of noise in the data were very low (the majority of the recorded reciprocal errors were <1%). This was due partly to imposing a maximum geometric factor on the configurations used in the survey design scheme (K_{max}), partly to the isolated rural location of the site, and partly to the low contact resistances (typically below a few hundred ohms) when the data were collected in December 2010. While a limiting K_{max} has been used successfully to reduce noise in real data in previous studies (Stummer *et al.* 2004; Loke *et al.* 2010a), a more sophisticated approach is to weight the data according to the error distribution (Blome *et al.* 2011). The expression for the linearised model resolution in eq. (2) then becomes

$$\mathbf{R} = ((\mathbf{W}_\mathrm{d}\mathbf{G})^\mathrm{T}(\mathbf{W}_\mathrm{d}\mathbf{G}) + \mathbf{C})^{-1}(\mathbf{W}_\mathrm{d}\mathbf{G})^\mathrm{T}(\mathbf{W}_\mathrm{d}\mathbf{G}), \tag{3}$$

where $\mathbf{W}_\mathrm{d}$ is the square-root of the a priori data covariance matrix (Miller & Routh 2007). We assume that the data are uncorrelated and contaminated by Gaussian noise with a voltage dependent standard deviation (Friedel *et al.* 2003). Since the subsurface resistivity distribution is assumed to be homogeneous at the design stage, the noise profile can be described by

$$\frac{\delta\rho_\mathrm{a}}{\rho_\mathrm{a}} = \varepsilon + \frac{K}{K_\mathrm{c}}, \tag{4}$$

where ρ_a is the apparent resistivity, ε is a constant background relative error level, K is the geometric factor and K_c is a characteristic geometric factor above which the data are predominantly random. Transforming to logarithmic data, $l = \ln\rho_\mathrm{a}$, the noise profile becomes

$$\delta l = \ln\left(1 + \varepsilon + \frac{K}{K_\mathrm{c}}\right). \tag{5}$$

In the standard formulation of the inverse problem, the *i*th diagonal entry of $\mathbf{W}_\mathrm{d}$ is then simply $1/\delta l_i$, where i labels the data.

To illustrate the effects of incorporating the noise distribution, we used the forward model shown in Figure 2b to generate synthetic data contaminated by noise as per eq. (4) with $\varepsilon = 0.015$ and $K_\mathrm{c} = 3.1 \times 10^5$ m. These parameters were characteristic of the errors in dipole-dipole monitoring data recorded at the landslide site in September 2010 when noise levels were significantly elevated due to higher contact resistances caused by the preceding dry summer. To compare the results of the dipole-dipole survey, the original CR survey and a new data-weighted CR survey, it was necessary to ensure that the same level of regularisation was applied (Blome *et al.* 2011). To this end, we scaled the data weighting by $\ln(1 + \varepsilon_\mathrm{mod})$ so that, for data

with noise levels greater than a specified cut-off (ε_{mod}), the diagonal entries of $\mathbf{W}_d$ became $\ln(1 + \varepsilon_{mod}) / \delta l_i$. The cut-off level was chosen to represent the level of modelling errors in the inversion (due to e.g. the finite discretisation of the differential equations and the approximation of the boundary conditions), and was set to $\varepsilon_{mod} = 0.01$. Any data with noise levels below ε_{mod} can be considered to be effectively equally precise with respect to the inversion and their corresponding diagonal entries of $\mathbf{W}_d$ are set to 1 (this does not occur in this synthetic example, but is relevant in the following field data example).

Using this data weighting, we recalculated the relative model resolution distributions for the dipole-dipole and original CR surveys (shown in Figure 12a and c). The resolution values are reduced in comparison with the equivalent noise-free plots shown in Figure 2c and e. This effect is more pronounced at greater depth, which is due to the decrease in data weighting with increasing geometric factor. The average resolution values decreased from $S = 0.629$ to $S = 0.512$ for the dipole-dipole survey and from $S = 0.717$ to $S = 0.548$ for the CR survey. We also ran the CR algorithm using the scaled data weighting to produce a data-weighted CR (DWCR) survey, which produced the relative model resolution plot shown in Figure 12e with an average resolution $S = 0.617$, greater than either the dipole-dipole or CR surveys. The DWCR survey contained configurations with significantly lower geometric factors than the other surveys (see Table 1) and therefore its resulting data had lower levels of noise.

Using the same noise profile, ten different noise-contaminated data sets were produced for each survey design. Representative inversions of a noisy data set for each survey are shown in Figure 12b (dipole-dipole), Figure 12d (CR) and Figure 12f (DWCR). It is clear that the dipole-dipole and CR survey images have been adversely

affected by the addition of noise, which has given rise to small scale artefacts and has impaired the recovery of the geometry and resistivity contrast of the blocks in comparison to the noise-free images, especially at depth. The average image quality measures for the noisy dipole-dipole data across the ten data sets have decreased to $P = 0.760 \pm 0.007$, $\Sigma = 0.727 \pm 0.008$ compared with $P = 0.825$, $\Sigma = 0.785$ for the noise-free image. Similarly the noisy CR images had $P = 0.761 \pm 0.011$, $\Sigma = 0.722 \pm 0.011$ compared with previous values of $P = 0.837$, $\Sigma = 0.794$. By contrast, the DWCR images are much less affected by the added noise. While the resistivity contrasts of the deeper blocks are not as quite as well recovered as in the noise-free cases, the images have few noticeable artefacts and the geometries of the blocks are more accurately recovered. The image quality measures are also significantly greater than for the noisy dipole-dipole or CR images ($P = 0.811 \pm 0.003$, $\Sigma = 0.767 \pm 0.002$). Lastly, the average RMS misfit error for the DWCR data was only 1.5%, compared to 2.7% for the dipole-dipole and 4.0% for the CR data. Generally, while all the noise-contaminated images are reduced in quality compared to Figure 2, the degradation has been minimised for the DWCR survey by incorporating the data-weighting into the survey design algorithm.

We also applied the DWCR algorithm to real data gathered at the landslide site in May 2011. At this time contact resistances were still low, with the exception of one electrode whose contact resistance rapidly increased during data collection. Data were initially obtained for the dipole-dipole and CR survey designs, and the noise levels were assessed from the reciprocal error estimates. These were fitted to a model noise distribution with $\varepsilon = 0.0015$ and $K_c = 1.6 \times 10^6$ m, which was used to design a DWCR survey as was done for the synthetic data above. The range of geometric factors and data weights for each survey are given in Table 2.

The model resolution distributions for the real dipole-dipole, CR and DWCR surveys are shown in Figure 13a-c. As with the synthetic data example, the model resolutions for the dipole-dipole and CR surveys ($S = 0.618$ and $S = 0.683$ respectively) were reduced in comparison with the noise-free examples. The model resolution for the DWCR survey was greater at $S = 0.711$. During data collection with these surveys we noted that the reciprocal errors of measurements involving the electrode at 123.5 m were increasing rapidly and that this was distorting the noise distributions. The electrode was found to have developed a high contact resistance, and any measurements involving it were removed from the data. This was taken into account when processing the reciprocal errors and when fitting the ε and K_c parameters to the noise distribution. The reciprocal error distributions, with the high contact resistance electrode excluded, are shown in Figure 13d-f for the three surveys. They demonstrate that the dipole-dipole data have the lowest overall noise levels and that the CR data have the highest, with the DWCR noise levels in between. This is consistent with the distributions of geometric factors in Table 2. The characteristics of the inverted images are consistent with the dipole-dipole and CR images obtained from the December 2010 data (Figure 8); the dipole-dipole image (Figure 13g) has failed to resolve the SSF/RMF boundary, but it is more clearly apparent in the CR and DWCR images (Figure 13h and i). Also, the resistivity contrasts in the CR and DWCR images are also somewhat greater than those in the dipole-dipole image. Since the overall noise levels are low, there are no obvious noise-induced artefacts in the CR image as there were in the synthetic example, and hence the CR and DWCR images are extremely similar. In this case, the quantifiable improvement resulting from using the data-weighted survey design is that the RMS misfit error between the inverted and measured data is reduced from 1.1% for the CR

survey to 0.9% (the same as for the dipole-dipole survey). These results demonstrate that, with both the synthetic and real data, using data weighting has enabled the optimisation algorithms to produce surveys which maintain image resolution in the presence of noise while reducing data errors and inversion misfit levels.

7 Conclusions

Synthetic model studies, in this work and others, have shown that optimal survey design algorithms for resistivity imaging produce significantly better image resolution than standard surveys. But if such surveys are to be applied practically in the field, considerations other than just maximising the predicted image resolution must be taken into account. In this paper we have addressed the problems of avoiding electrode polarisation effects, making efficient use of parallel measurement channels, and making optimal measurements in noisy environments. We demonstrated our methods using synthetic and real data from survey designs generated by the "Compare *R*" algorithm, although the solutions we have presented should be easily adaptable to other optimal design methods.

To eliminate electrode polarisation effects, we implemented a general method to reorder arbitrary resistivity imaging arrays. Using a random array as a test case, we designed a simulated annealing scheme to maximise the separation in time between electrodes being used to transmit current and measure potential, hence minimising electrode polarisation. Our results showed that polarisation errors can be effectively eliminated from real data measured using optimised surveys in either single- or multi-channel acquisition modes.

We implemented multi-channel optimisation by adapting the original algorithm to design surveys sequentially by multi-channel commands instead of by

single channel electrode configurations. This introduces additional constraints to the design process: all configurations in a given command share the same pair of current electrodes; adjacent configurations share a common potential electrode; and no potential electrode can occur more than once in a given command. The resulting model resolution distributions and inverted images were nearly as close to optimal as those produced by the single channel surveys. Critically the acquisition of real data using these arrays is an order-of-magnitude faster than in single channel operation, making the multi-channel survey designs better suited to monitoring dynamic subsurface processes on rapid timescales.

To account for the effects of noise on image resolution, we weighted the data using a simple noise model consisting of a constant background noise level and a term dependent on the geometric factor of the measurement. This caused the optimisation algorithm to preferentially select measurement configurations with lower geometric factors, and hence higher return voltages and lower susceptibility to noise. Results from synthetic and real data showed that, in the presence of noise, this resulted in better image resolution and improved agreement between the measured and inverted data.

When using data weighting, it is important to have an accurate model of the noise profile; too much damping reduces the contrast in the image while too little gives rise to artefacts (Labrecque *et al.* 1996), both situations that at least partially negate the demonstrated advantages of using optimised surveys. We made the simplifying assumption of a homogeneous half-space resistivity to model the distribution of noise, thereby allowing us to express the noise as a function of geometric factor rather than voltage. Using a more accurate resistivity distribution when calculating the model resolution has been shown to have little effect on the

performance of the type of optimisation algorithms discussed in this paper (Stummer *et al.* 2004). However, prior knowledge of the resistivity distribution could be used to calculate the expected voltages for given measurement configurations and hence weight them more accurately in the optimisation. This could further improve results for some of the field examples given in this paper, where the near-surface resistivities vary by an order-of-magnitude.

Another consideration, which we have not addressed in this paper, is how to design a multi-channel survey whose reciprocal configurations can also be measured efficiently in multi-channel operation. One of the advantages of the dipole-dipole survey is that its reciprocal measurements can be organised to make as efficient use of multiple acquisition channels as the normal measurements. In this study we had to gather all corresponding reciprocal data for our optimised multi-channel field examples in single-channel mode. Reciprocal measurement pairs are particularly useful for assessing noise distributions, transient data errors and problematic electrodes. Unlike repeat measurements, they can also identify systematic errors such as electrode polarisation (Labrecque *et al.* 1996). While noise distribution models could be determined by measuring the potential across a given bipole for a range of injection currents, care would have to be taken to obtain data over a variety of positions and depths of investigation. Problematic electrodes might be identified by contact resistance measurements, and polarisation effects can be minimised using the techniques described in this paper. But even in combination, these alternative methods do not have the desirable property of measuring the levels of both random and systematic noise in the actual data used in the inversion. Therefore a substantial challenge for future work to address is the efficient multi-channel measurement of forward and reciprocal data in optimised ERT survey design.

Finally, in this paper we have been predominantly interested in designing surveys for general use (e.g. when little or no prior information is available). Hence we used a homogeneous half-space model for calculating the sensitivities and noise models, and aimed to maximise the relative model resolution evenly across the image space. In future work we will study optimisation for time-lapse monitoring, which will incorporate prior estimates of the subsurface resistivity distribution, more accurate noise models, and will focus the optimisation on regions of the subsurface where significant changes are occurring.

Acknowledgements

References

Blome M., Maurer, H. & Greenhalgh, S., 2011. Geoelectric experimental design – Efficient acquisition and exploitation of complete pole-bipole data sets, *Geophysics*, **76**, F15–F26.

British Geological Survey, 1983. *York Solid and Drift (Sheet 63). 1:50 000.* Ordnance Survey for Institute of Geological Sciences, Southampton UK.

Chambers. J.E., Wilkinson, P.B., Kuras, O., Ford, J.R., Gunn, D.A., Meldrum, P.I., Penningtion, C.V.L., Weller, A.L., Hobbs, P.R.N. & Ogilvy, R.D., 2011. Three-dimensional geophysical anatomy of an active landslide in Lias Group mudrocks, Cleveland Basin, UK, *Geomorphology*, **125**, 472–484.

Coles, D.A. & Morgan F.D., 2009. A method of fast, sequential experimental design for linearized geophysical inverse problems, *Geophys. J. Int.*, **178**, 145–158.

Dahlin, T., 2000. Short note on electrode charge-up effects in DC resistivity data acquisition using multi-electrode arrays, *Geophys. Prospect.*, **48**, 181–187.

Friedel, S., 2003. Resolution, stability and efficiency of resistivity tomography estimated from a generalized inverse approach, *Geophys. J. Int.*, **153**, 305–316.

Furman, A., Ferré, T.P.A. & Warrick, A.W., 2004. Optimization of ERT surveys for monitoring transient hydrological events using perturbation sensitivity and genetic algorithms, *Vadose Zone J.*, **3**, 1230–1239.

Furman, A., Ferre, T.P.A. & Heath, G.L., 2007. Spatial focusing of electrical resistivity surveys considering geologic and hydrologic layering, *Geophysics*, **72**, F65–F73.

Goto, K. & van de Geijn, R. A., 2008. Anatomy of high-performance matrix multiplication, *ACM Transactions on Mathematical Software*, **34**, art. 12.

LaBrecque, D.J., Miletto, M., Daily, W., Ramirex, A. & Owen, E., 1996. The effects of noise on Occam's inversion of resistivity tomography data, *Geophysics*, **61**, 538-548.

Lehmann, H., 1995. Potential representation by independent configurations on a multielectrode array, *Geophys. J. Int.*, **120**, 331–338.

Loke, M.H., Acworth, I. & Dahlin, T., 2003. A comparison of smooth and blocky inversion methods in 2D electrical imaging surveys, *Explor. Geophys.*, **34**, 182–187.

Loke, M.H., Wilkinson, P.B. & Chambers, J.E., 2010a. Fast computation of optimized electrode arrays for 2D resistivity surveys, *Computers & Geosciences*, **36**, 1414–1426.

Loke, M.H., Wilkinson, P.B. & Chambers, J.E., 2010b. Parallel computation of optimized arrays for 2-D electrical imaging surveys, *Geophys. J. Int.*, **183**, 1302–1315.

Maurer, H. & Friedel, S., 2006. Outer-space sensitivities in geoelectrical tomography, *Geophysics*, **71**, G93–G96.

Maurer, H., Curtis, A. & Boerner D.E., 2010. Recent advances in optimized geophysical survey design, *Geophysics*, **75**, 75A177–75A194.

Menke, W., 1989. *Geophysical Data Analysis: Discrete Inverse Theory,* Rev. ed., Academic Press, Inc., San Diego, CA.

Merriam, J.B., 2005. Injection electrode overprinting, *J Environ. Eng. Geophys.*, **10**, 365–370.

Miller, C.R. & Routh, P.S., 2007. Resolution analysis of geophysical images: Comparison between point spread function and region of data influence measures, *Geophys. Prospect.*, **55**, 835–852.

Parasnis, D.S., 1988. Reciprocity theorems in geoelectric and geoelectromagnetic work, *Geoexploration*, **25**, 177–198.

Press, W.H., Teukolsky, S.A., Vetterling, W.T. & Flannery, B.P., 1992. *Numerical Recipes in C: The Art of Scientific Computing*, 2nd ed., Cambridge University Press, Cambridge.

Stummer, P., Maurer, H. & Horstmeyer, H. & Green, A.G., 2002. Optimization of DC resistivity data acquisition: Real-time experimental design and a new multielectrode system, *IEEE Transactions on Geoscience and Remote Sensing*, **40**, 2727–2735.

Stummer, P., Maurer, H. & Green, A.G., 2004. Experimental design: Electrical resistivity data sets that provide optimum subsurface information, *Geophysics*, **69**, 120–139.

Wang, Z. & Sheikh, H.R., 2004. Image quality assessment: From error visibility to structural similarity, *IEEE Transactions on Image Processing*, **13**, 600–612.

Wilkinson, P.B., Meldrum, P.I., Chambers, J.E., Kuras, O. & Ogilvy R.D., 2006a. Improved strategies for the automatic selection of optimized sets of electrical resistivity tomography measurement configurations, *Geophys. J. Int.*, **167**, 1119–1126.

Wilkinson, P.B., Kuras, O., Meldrum, P.I., Chambers, J.E. & Ogilvy R.D., 2006b. Comparison of the spatial resolution of standard and optimised electrical resistivity tomography arrays, in *Proceedings 12th EAGE Near Surf. Geophys. Meeting*, Helsinki, Finland.

Wilkinson, P.B., Chambers, J.E., Meldrum, P.I., Gunn, D.A., Ogilvy, R.D. & Kuras, O., 2010. Predicting the movements of permanently installed electrodes on an active landslide using time-lapse geoelectrical resistivity data only, *Geophys. J. Int.*, **183**, 543–556.

Zhe, J., Greenhalgh, S. & Marescot, L., 2007. Multichannel, full waveform and flexible electrode combination resitivity-imaging system, *Geophysics*, **72**, F57-F64.

Table 1. Geometric factors (K) and data weights for synthetic data using a noise model with $\varepsilon = 0.015$, $K_c = 3.1 \times 10^5$ m.

K position	Dipole-dipole		CR		DWCR	
	K (m)	Weight	K (m)	Weight	K (m)	Weight
Min	90	0.66	45	0.66	45	0.66
Quartile 1	716	0.58	895	0.56	851	0.57
Median	3134	0.40	5014	0.32	1680	0.49
Quartile 3	9401	0.22	24661	0.11	2403	0.44
Max	39396	0.07	39396	0.07	5014	0.32

Table 2. Geometric factors (K) and data weights for real data using a noise model with $\varepsilon = 0.0015$, $K_c = 1.6 \times 10^6$ m.

K position	Dipole-dipole		CR		DWCR	
	K (m)	Weight	K (m)	Weight	K (m)	Weight
Min	90	1.00	45	1.00	60	1.00
Quartile 1	716	1.00	895	1.00	895	1.00
Median	3134	1.00	5014	1.00	3581	1.00
Quartile 3	9401	1.00	24661	0.59	11482	1.00
Max	39396	0.39	39396	0.39	15343	0.90
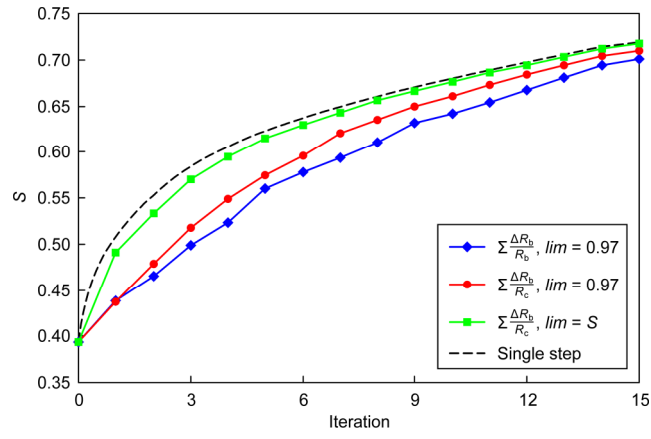
Figure 1. Optimisation performance in terms of average relative model resolution S for three variants of the CR algorithm compared with the single step algorithm.
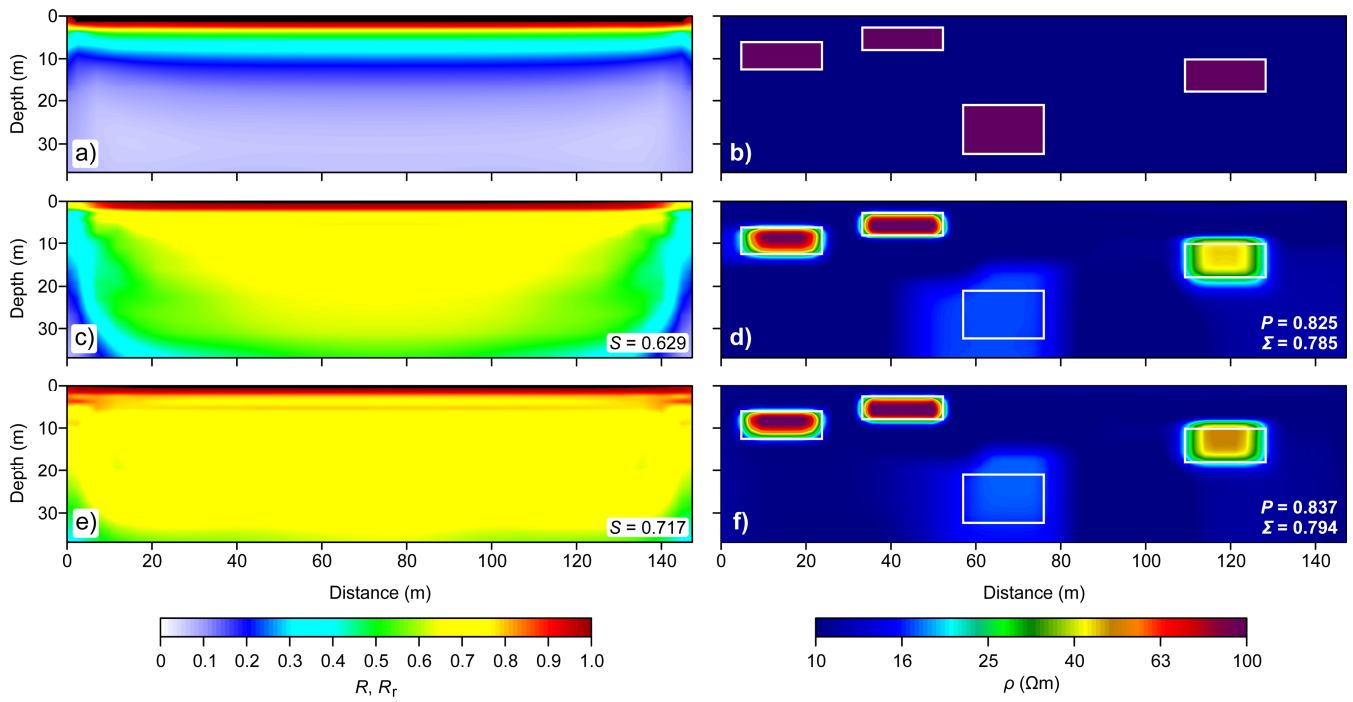
Figure 2. a) Model resolution distribution R for the comprehensive measurement set. b) Forward model used to generate synthetic data. c) Relative model resolution R_r for the dipole-dipole survey. d) Inverted resistivity image from dipole-dipole data. e) Relative model resolution R_r for the CR survey. f) Inverted resistivity image from CR data. Also shown are average resolution values S and correlation and structural similarity coefficients (P and Σ).
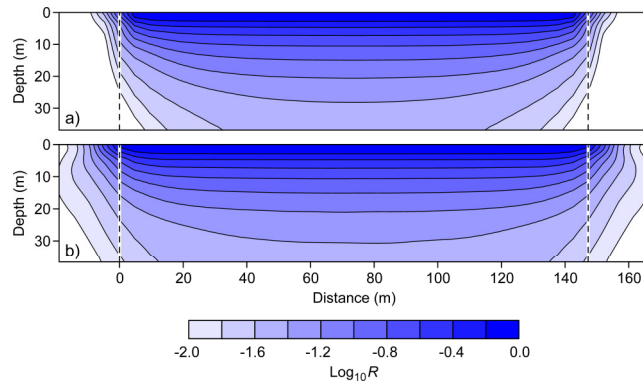
Figure 3. Model resolution distributions for a) the dipole-dipole survey and b) the CR survey. The dashed lines indicate the ends of the linear electrode array. The "outer-space" regions extend by four electrode spacings beyond the dashed lines.
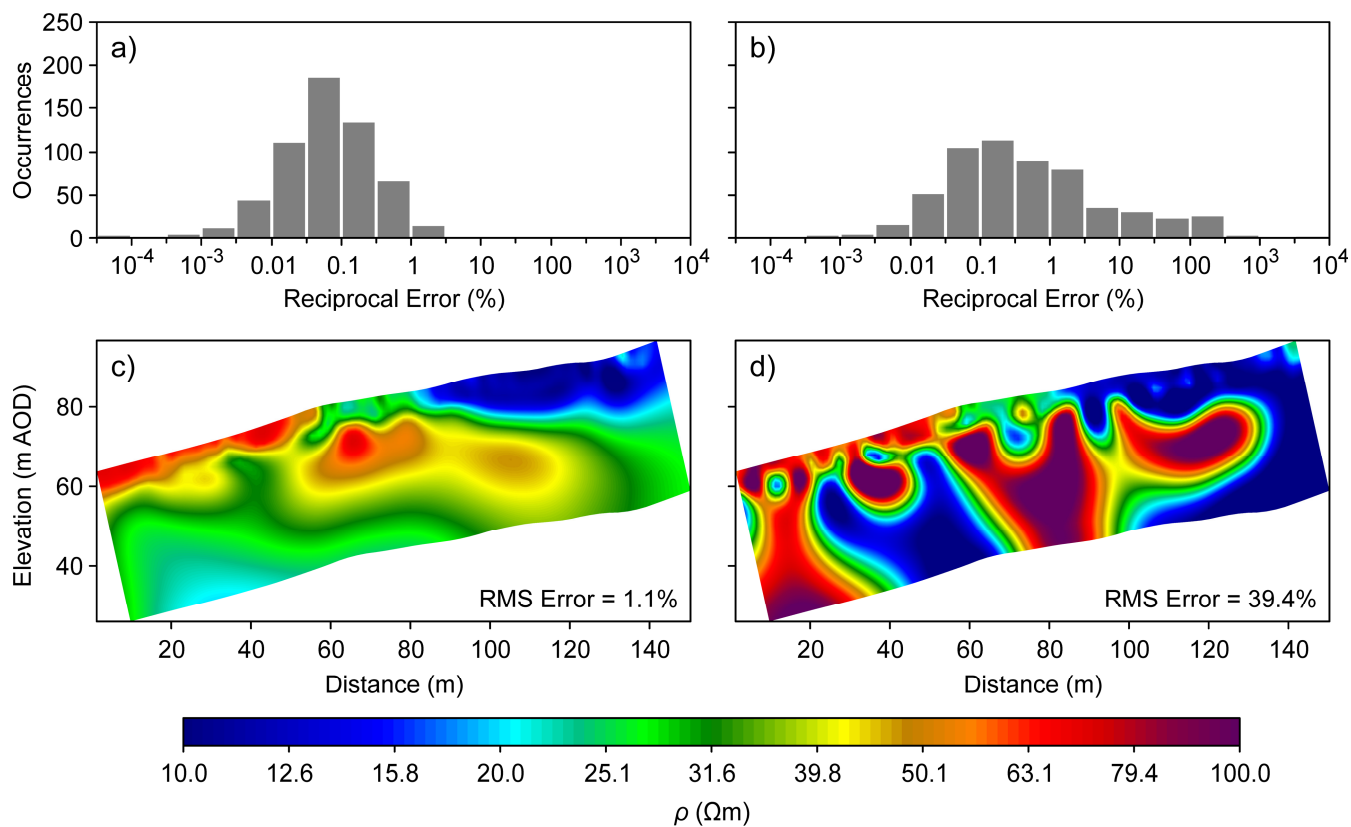
Figure 4. Distributions of reciprocal errors for a) the dipole-dipole survey and b) the CR survey before rearrangement to avoid polarisation effects. The resulting resistivity images and RMS misfit errors are shown in c) and d) respectively.
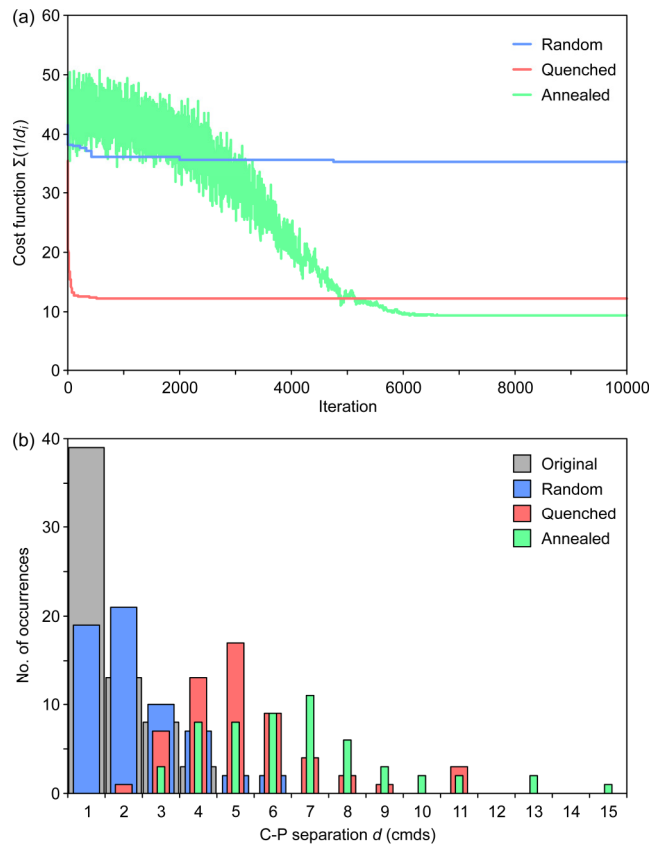
Figure 5. a) Costs of rearranging a random survey as a function of iteration for three minimisation strategies. b) Resulting distributions of C-P separations.
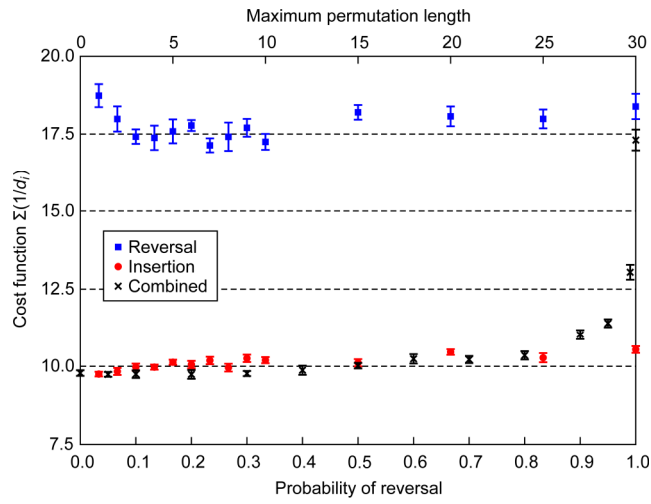
Figure 6. Minimum cost function values achieved using reversals (blue squares), moves (red circles) and in combination (black crosses). The error bars show the standard error in the means. Note that the length of a reversed/moved section excludes/includes the first command respectively.
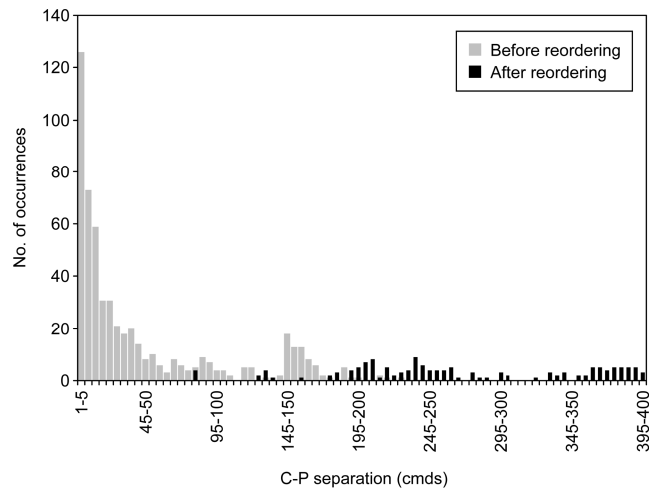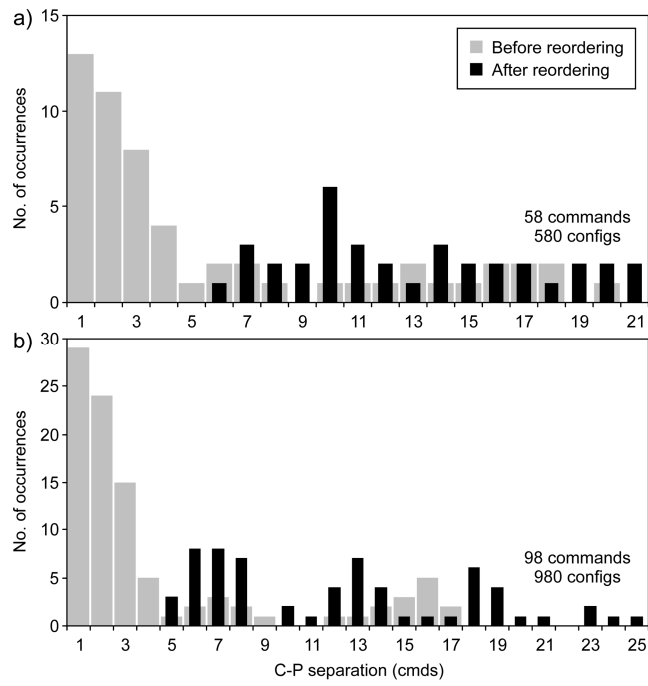
Figure 7. Distribution of C-P separations for the CR survey, before and after rearrangement using simulated annealing.
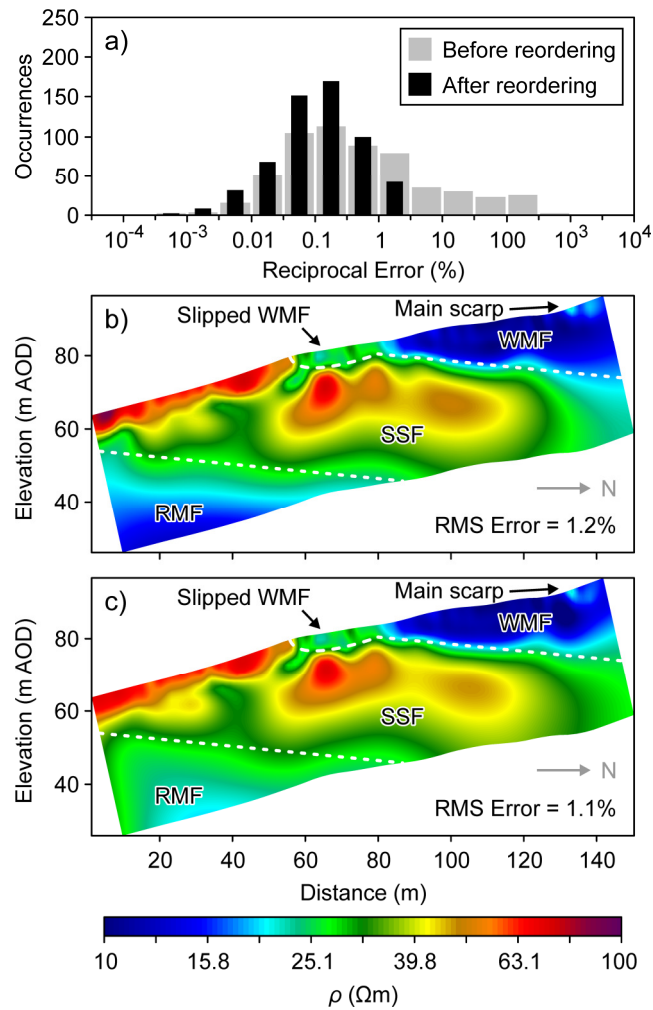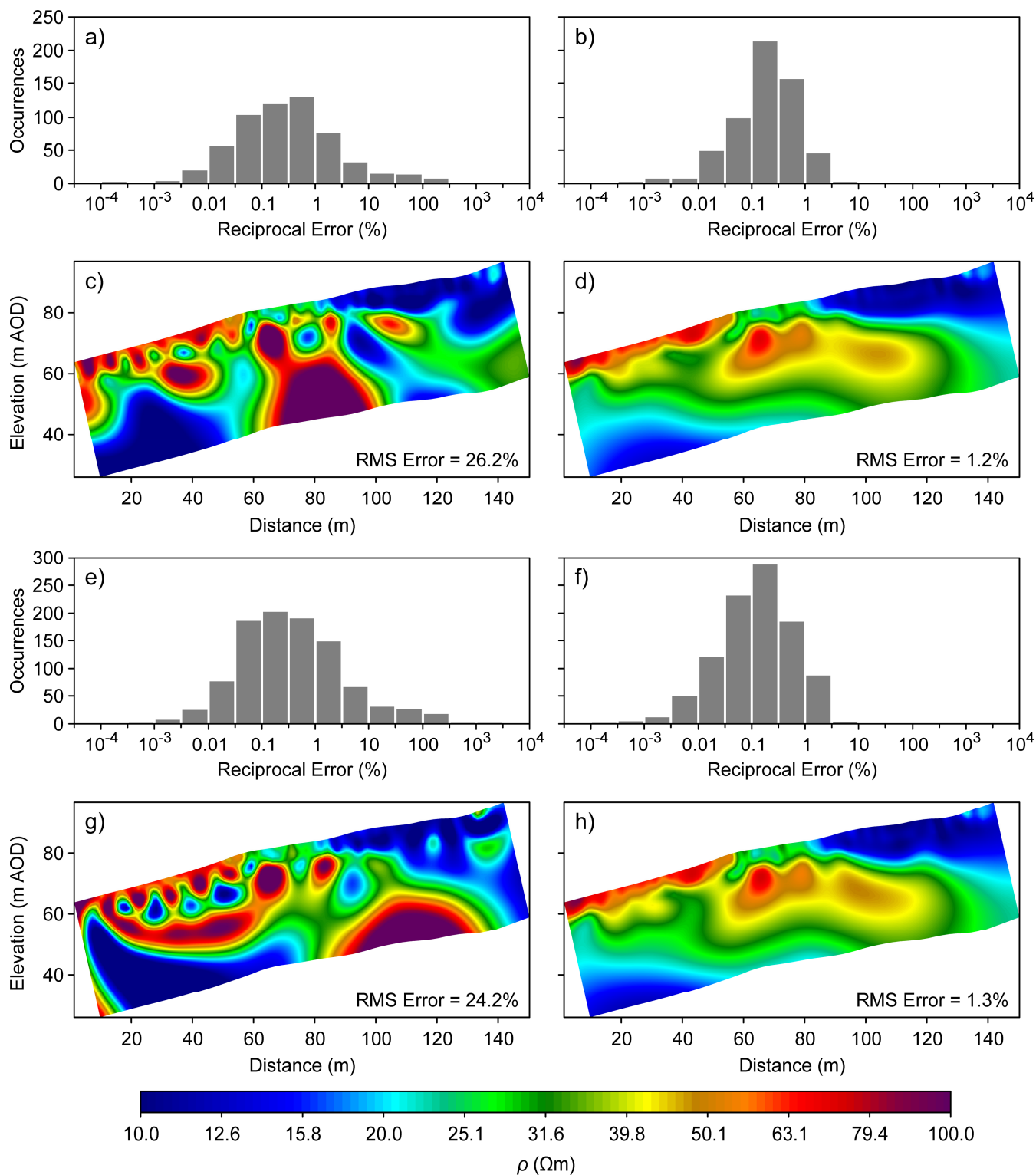
Figure 8. a) Distributions of reciprocal errors for the CR survey before (grey) and after (black) rearrangement to avoid polarisation effects. The resistivity image from the reordered CR survey and its RMS misfit error are shown in b) with the equivalent results of the dipole-dipole survey shown in c) for comparison. The inferred boundaries between the Whitby (WMF), Staithes (SSF) and Redcar (RMF) formations are shown by dashed white lines. The main scarp and slipped Whitby material are indicated by black arrows. North is indicated by grey arrows.
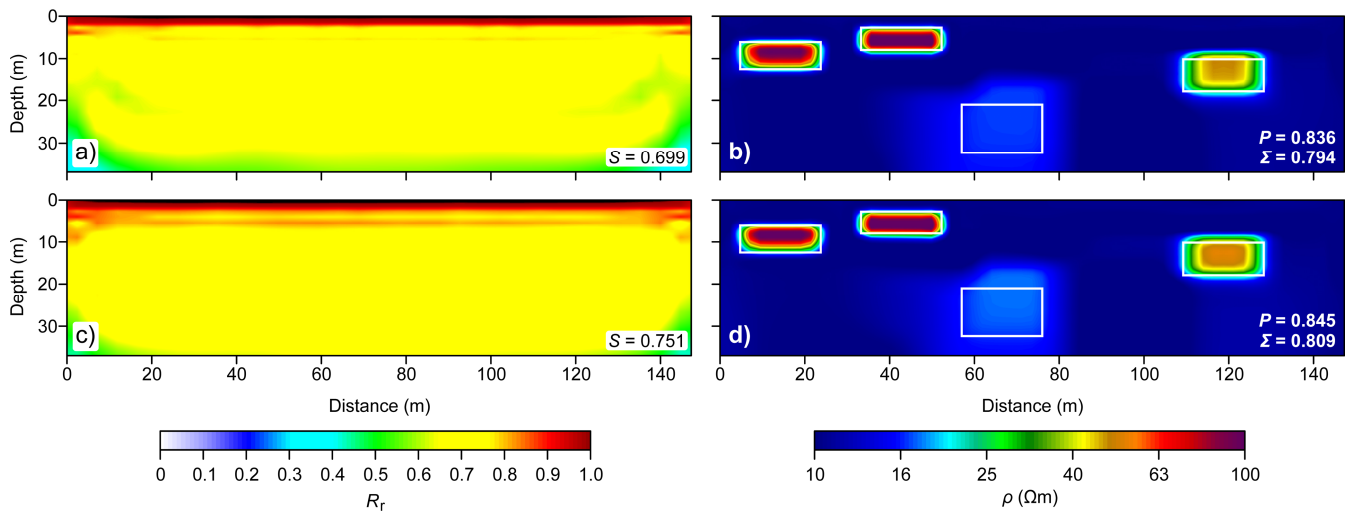
Figure 9. a) R_r distribution for the 58-command multi-channel MCCR survey. b) Inverted resistivity image from 58-command MCCR data. c) R_r distribution for the 98-command multi-channel MCCR survey. d) Inverted resistivity image from 98-command MCCR data. Also shown are average resolution values S and correlation and structural similarity coefficients (P and Σ).

Figure 10. Distribution of C-P separations for a) the 58-command and b) the 98-command MCCR surveys, before and after rearrangement using simulated annealing.
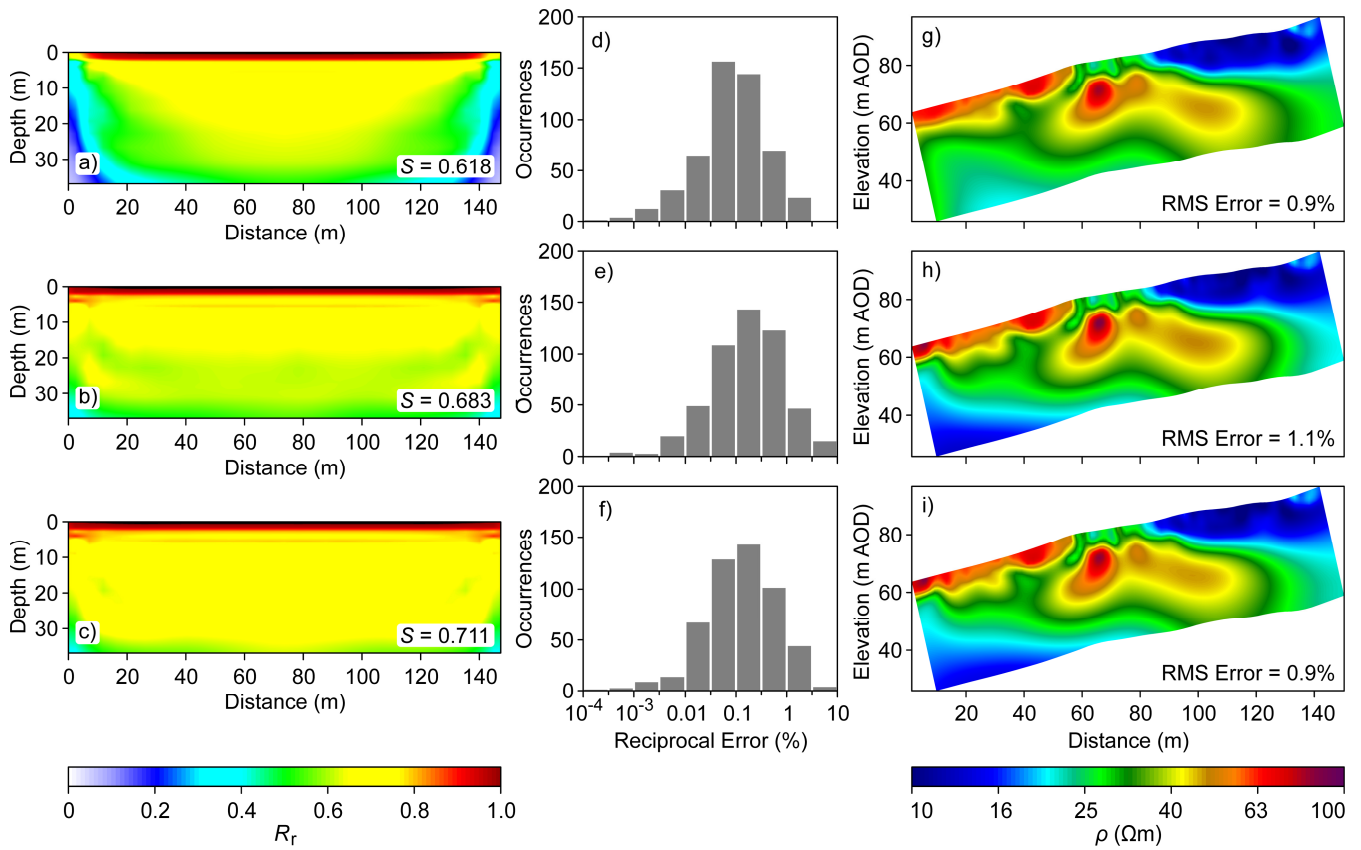
Figure 11. Distributions of reciprocal errors for the 58-command MCCR survey a) before and b) after rearrangement to avoid polarisation effects. The resulting resistivity images and RMS misfit errors are shown in c) and d) respectively. Equivalent results for the 98-command MCCR survey are shown in e)-h).
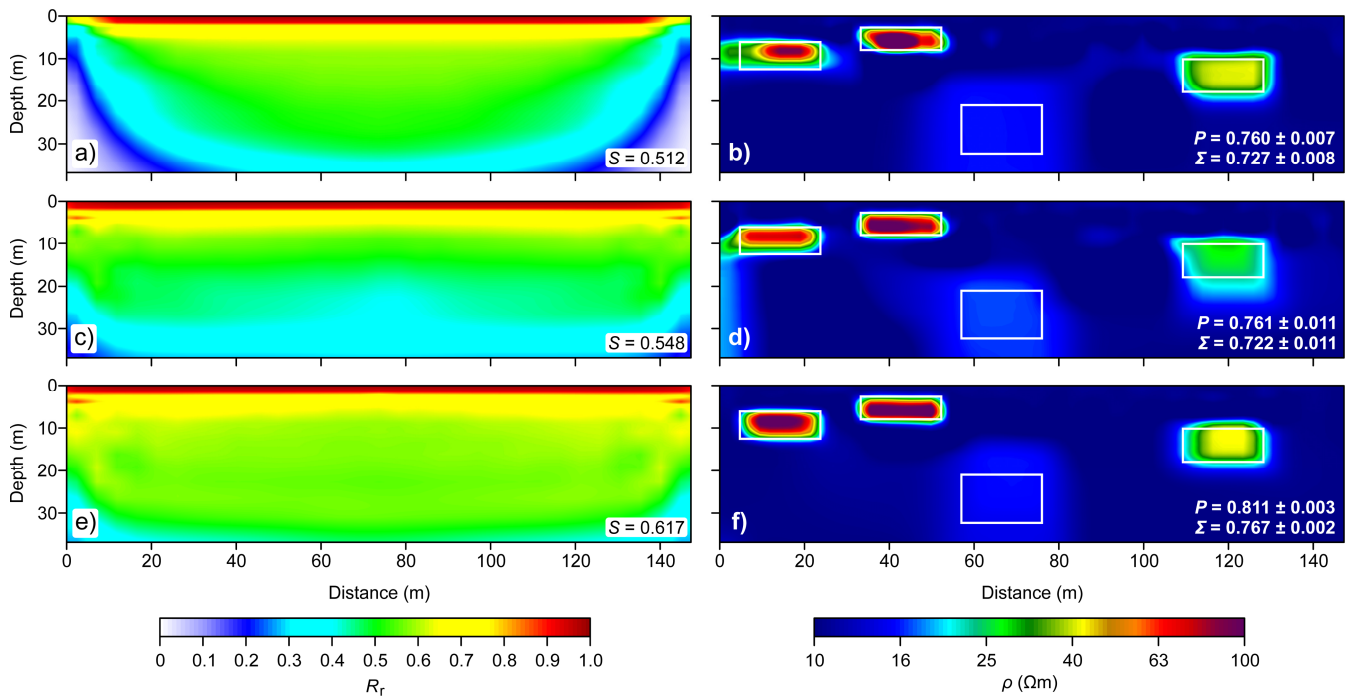
Figure 12. a) Data-weighted relative model resolution distribution R_r for the dipole-dipole survey. b) Representative inverted resistivity image from noisy synthetic dipole-dipole data. c) Data-weighted R_r distribution for the original CR survey. d) Representative inverted resistivity image from noisy CR data. e) Data-weighted R_r distribution for the data-weighted DWCR survey. f) Representative inverted resistivity image from noisy DWCR data. Also shown are average resolution values S and estimated correlation and structural similarity coefficients (P and Σ, averaged over ten images).

Figure 13. a)-c) Data-weighted relative model resolution distributions R_r for the dipole-dipole, original CR and data-weighted DWCR surveys. Also shown are average resolution S values. d)-f) Reciprocal error distributions for dipole-dipole, CR and DWCR data. g)-i) Inverted resistivity images and RMS misfit errors from dipole-dipole, CR and DWCR data.